Astronomy & Astrophysics

Modelling the spectral energy distribution of galaxies

IV. Correcting apparent disk scalelengths and central surface brightnesses for the effect of dust at optical and near-infrared wavelengths[*]

C. Möllenhoff[1], C. C. Popescu[2,3,4], and R. J. Tuffs[2,3]

[1] Zentrum für Astronomie der Universität Heidelberg, Landessternwarte, Königstuhl 12, 69117 Heidelberg, Germany
   e-mail: cmoellen@lsw.uni-heidelberg.de
[2] Max-Planck-Institut für Kernphysik, Saupfercheckweg 1, 69117 Heidelberg, Germany
   e-mail: [Cristina.Popescu;Richard.Tuffs]@mpi-hd.mpg.de
[3] The Observatories of the Carnegie Institution of Washington, 813 Santa Barbara St., Pasadena, CA 91101, USA
[4] Research Associate, The Astronomical Institute of the Romanian Academy, Str. Cuţitul de Argint 5, Bucharest, Romania

ABSTRACT

We present corrections for the change in the apparent scalelengths, central surface brightnesses and axis ratios due to the presence of dust in pure disk galaxies, as a function of inclination, central face-on opacity in the B-band (τ_B^f) and wavelength. The correction factors were derived from simulated images of disk galaxies created using geometries for stars and dust which can reproduce the entire spectral energy distribution from the ultraviolet (UV) to the Far-infrared (FIR)/submillimeter (submm) and can also account for the observed surface-brightness distributions in both the optical/Near-infrared and FIR/submm. We found that dust can significantly affect both the scalelength and central surface brightness, inducing variations in the apparent to intrinsic quantities of up to 50% in scalelength and up to 1.5 mag in central surface brightness. We also identified some astrophysical effects for which, although the absolute effect of dust is non-negligible, the predicted variation over a likely range in opacity is relatively small, such that an exact knowledge of opacity is not needed. Thus, for a galaxy at a typical inclination of 37° and having any $\tau_B^f > 2$, the effect of dust is to increase the scalelength in B relative to that in I by a factor of 1.12 ± 0.02 and to change the $B - I$ central colour by 0.36 ± 0.05 mag. Finally we use the model to analyse the observed scalelength ratios between B and I for a sample of disk-dominated spiral galaxies, finding that the tendency for apparent scalelength to increase with decreasing wavelength is primarily due to the effects of dust.

Key words. galaxies: spiral – galaxies: structure – galaxies: photometry – galaxies: fundamental parameters – ISM: dust, extinction – radiative transfer

1. Introduction

A primary goal of modern studies of star-forming galaxies is to understand how these systems were assembled over cosmic time. If the disks of spiral galaxies grow from the inside out, as predicted by semi-analytical hierarchical models for galaxy formation (e.g. Mo et al. 1998), one would predict the stellar populations to be younger and have lower metallicity in the outer disk than in the inner disk, such that local universe galaxies should be intrinsically larger at the shorter wavelengths where light from the young stellar population is more prominent. For the same reason one would expect the intrinsic sizes of spiral disks to be larger at the current epoch than at higher redshift. Observationally, such predictions can be tested in two ways. One way is to compare the spatial distribution of the constituent stellar populations at different wavelengths, for local universe galaxies. Another way is to look for structural differences in galaxies observed at different cosmological epochs, at the same rest frame wavelength. Both methods require an analysis of the surface-brightness distribution of spiral galaxies in the optical and near-infrared (NIR) to quantify the distribution of starlight, for

example by deriving the scalelength of the disk. This is done by fitting observed images with models for the surface-brightness distribution of stellar light, whereby the disk component is usually specified by an exponential distribution. The derived exponential scalelengths can either be intercompared between different wavelengths for local universe galaxies (Elmegreen & Elmegreen 1984; Peletier et al. 1994; Evans 1994; De Jong 1996a,b; de Grijs 1998; Cunow 1998, 2001, 2004; MacArthur et al. 2003; Möllenhoff 2004), or between galaxies at different redshifts at a given wavelength (Lilly et al. 1998; Simard et al. 1999; Ravindranath et al. 2004; Trujillo & Aguerri 2004; Trujillo et al. 2005; Barden et al. 2005). However, the appearance of disk galaxies is strongly affected by dust and this effect is different at different wavelengths and for different opacities. This has consequences not only for the derivation of the variation of intrinsic scalelength with wavelength, but also for the variation of intrinsic scalelength with cosmological epoch, since the opacity of disk galaxies is expected to have been systematically higher in the past (e.g. Dwek 1998; Pei et al. 1999).

The effect of dust on the observed scalelengths and central surface brightnesses of disk galaxies has been previously modelled by Byun et al. (1994), Evans (1994) and Cunow (2001). By means of radiative transfer calculations these works

---

[*] Tables 1 to 5 are only available in electronic form at http://www.edpsciences.org

investigated the dependence of this effect on star/dust geometry, opacity, inclination and wavelength. Recently, a better knowledge of the star/dust geometry has been obtained through a joint consideration of the direct starlight, emitted in the ultraviolet (UV)/optical/NIR, and of the starlight which is re-radiated in the Far-infrared (FIR)/submillimeter (submm). In a series of papers devoted to modelling the spectral energy distributions (SEDs) we derived geometries of the distribution of stellar light and dust that are successful in reproducing not only the observed integrated SEDs, but also the observed radial profiles both in the optical/NIR and FIR/submm (Popescu et al. 2000, hereafter Paper I; Misiriotis et al. 2001, hereafter Paper II; Popescu et al. 2004; see also Popescu & Tuffs 2005[1]).

In this paper, the fourth in this series, we use these derived distributions of stars and dust to obtain a new quantitative measure of the effect of dust on the observed photometric parameters in the optical wavebands. Furthermore, because it is no longer necessary to explore a wide range of star/dust geometries, we are also able to systematically explore the full parameter space in opacity, inclination and wavelength, and tabulate the results in a form convenient for the use of the community. We give quantitative measures of the change in the apparent scalelength, central surface brightnesses and inclination of disk galaxies due to the presence of dust[2]. All these changes are expressed as the ratio of the apparent quantity (i.e. that obtained by fitting images of dusty disks with pure exponential disks) to the intrinsic quantity (i.e. that which would be obtained in the absence of dust). These corrections have been derived from a subset of the simulated images (those in the optical bands) presented in Tuffs et al. (2004, hereafter Paper III).

In Sect. 2 we give a brief description of the distributions of stars and dust used in the simulated images. In Sect. 3 we specify the fitting procedure used to extract apparent scalelengths, central surface brightnesses and axis ratios from the simulated images. These quantities are tabulated in Sect. 4, where we also describe and explain their dependence on opacity, inclination and wavelength due to the effect of dust. In Sect. 5 we examine the impact of these new results on our ability to derive quantities of astrophysical interest from optical observations and give in Sect. 6 a specific example of the determination of the variation of intrinsic scalelength with wavelength for local universe galaxies. A summary of the paper is given in Sect. 7.

2. The simulated images

In Paper III we presented simulated images for the diffuse component of a spiral galaxy. This diffuse component is comprised of a diffuse old stellar population and associated dust and a diffuse young stellar population and associated dust. Direct evidence for the existence of the diffuse dust disk is provided by images of FIR emission in spiral galaxies (for example in M 31 by Haas et al. 1998 and in M 33 by Hippelein et al. 2003), which clearly show a diffuse disk of cold dust emission prominent at $170\,\mu$m. FIR measurements of a statistically unbiased optically selected sample of gas-rich galaxies (Tuffs et al. 2002a,b) have shown that this diffuse cold dust emission component is ubiquitous along the Hubble sequence of late-type galaxies, and

carries the bulk of the dust luminosity for most of these systems (Popescu et al. 2002). It is thus responsible for most of the attenuation of the stellar light and the associated modification of disk brightness and scalelength measured in the optical, which is the subject of this paper.

We know that in reality the apparently diffuse dust component may itself have some structure, and that some fraction (currently unconstrained by direct observation) may be contained in clumps which are externally heated and have no embedded sources, the so-called "passive clumps" (Popescu & Tuffs 2005). However, providing these passive clumps are optically thin, the attenuation characteristics will be almost identical to those of a completely homogeneous distribution (Kuchinski et al. 1998; Pierini et al. 2004). If the passive clumps are considered to be optically thick, then the overall attenuation of a galaxy can be reduced by up to 40% (Bianchi et al. 2000a; Misiriotis & Bianchi 2002). But, once UV photons can no longer penetrate a clump, the photoelectric heating of the gas is lost and there is nothing to prevent the clump collapsing to form stars. This means that in practice optically thick passive clumps should not exist as stable long-lived structures, but rather as transient precursors of star-forming clouds. Once the star-formation is underway, the clumps will start to contain embedded sources, becoming "active" clumps (Popescu & Tuffs 2005). In terms of the global attenuation of stellar light in galaxies, the main effect of active clumps is to locally absorb a fraction of the UV output from the embedded massive stars and transform it into warm dust emission. This is taken into account by the model of Popescu et al. (2000) used in this series of papers. Active clumps have such a small filling factor in normal spiral galaxies that their effect on the propagation of the long-range optical/NIR photons in galaxy disks is negligible. Since in this paper we only consider the optical/NIR spectral range, it is only necessary here to take into account the diffuse dust distribution.

The diffuse old stellar population has both a "bulge" and a "disk" component, whereas the diffuse young stellar population resides only in a "thin disk". Here we only use the disk component, since in this paper we are only concerned with the appearance of the disk in the optical/NIR range. The simulations for the disk were performed taking the geometry of the diffuse dust to be the superposition of the dust in the disk and the dust in the thin disk. In other words the attenuated images represent the appearance of the stellar populations in the disk as seen through the dust in the disk and thin disk. The stellar emissivity of the disk η and the extinction coefficients of the dust associated with the disk, $\kappa_{\rm ext}^{\rm disk}$, and with the thin disk, $\kappa_{\rm ext}^{\rm tdisk}$, are described by exponentials:

$$\eta(\lambda, R, z) = \eta^{\rm disk}(\lambda, 0, 0) \exp\left(-\frac{R}{h_{\rm s}^{\rm disk}} - \frac{|z|}{z_{\rm s}^{\rm disk}}\right) \tag{1}$$

$$\kappa_{\rm ext}^{\rm disk}(\lambda, R, z) = \kappa_{\rm ext}^{\rm disk}(\lambda, 0, 0) \exp\left(-\frac{R}{h_{\rm d}^{\rm disk}} - \frac{|z|}{z_{\rm d}^{\rm disk}}\right) \tag{2}$$

$$\kappa_{\rm ext}^{\rm tdisk}(\lambda, R, z) = \kappa_{\rm ext}^{\rm tdisk}(\lambda, 0, 0) \exp\left(-\frac{R}{h_{\rm d}^{\rm tdisk}} - \frac{|z|}{z_{\rm d}^{\rm tdisk}}\right) \tag{3}$$

where R and z are the cylindrical coordinates, $\eta^{\rm disk}(\lambda, 0, 0)$ is the stellar emissivity at the centre of the disk, $h_{\rm s}^{\rm disk}$ and $z_{\rm s}^{\rm disk}$ are the scalelength and scaleheight of the stellar emissivity of the disk, $\kappa_{\rm ext}^{\rm disk}(\lambda, 0, 0)$ is the extinction coefficient at the centre of the disk, $h_{\rm d}^{\rm disk}$ and $z_{\rm d}^{\rm disk}$ are the scalelength and scaleheight of the dust

---

associated with the disk, $\kappa_{\text{ext}}^{\text{tdisk}}(\lambda, 0, 0)$ is the extinction coefficient at the centre of the thin disk and $h_{\text{d}}^{\text{tdisk}}$ and $z_{\text{d}}^{\text{tdisk}}$ are the scalelength and scaleheight of the dust associated with the thin disk. The values of these parameters are given in Tables 1 and 2 from Paper III. For the old stellar population and associated dust the values of these parameters were taken from the modelling of Xilouris et al. (1999). It should be noted that the thin disk of dust is an approximation to the distribution of dust associated with the spiral arms, as explained in Paper I, II and III. This approximation will be a better representation of spirals having multiple spiral arms covering a large fraction of the disk than of spirals having a two arm pattern with low coverage of the disk or of spirals with a ring structure. This may introduce some noise in the attenuation characteristics, in particular at the longest NIR wavelength, where the true relative geometry of stars and dust may differ the most from that assumed by the model. However it is at these wavelengths that attenuation is the least severe. It should also be noted that the geometry used by our model is only valid for massive (non-dwarf) spiral galaxies, for which Dalcanton et al. (2004) have suggested that disk instabilities lead to a thin dust layer through collapse and fragmentation of high density gas within spiral arms. For low-mass galaxies with circular velocities of less than 120 km s^{-1} Dalcanton et al. (2004) have shown that the disk has a different structure, with the dust having a larger scaleheight with respect to the stars than in more massive, spiral, galaxies.

The simulated images of the disk were calculated using the radiative transfer code of Kylafis & Bahcall (1987), which includes anisotropic multiple scattering in which the higher orders of scattered light are calculated using the method of "scattered intensities" (see also Kylafis & Xilouris 2005). The images have a pixel size (equal to the resolution) of 0.0066 of the B-band scalelength $h_{\text{s}}^{\text{disk}}$ and were sampled every 5 and 10 pixels in the inner and outer disk, respectively. They extend out to a radius of 4.63 B-band scalelengths $h_{\text{s}}^{\text{disk}}$, which is equivalent to 3.31 dust scalelengths $h_{\text{d}}^{\text{disk}}$. Examples of simulated disk images are shown in Fig. 1 from Paper III.

Here we make use of a subset of 280 of the simulated disk images presented in Paper III, spanning 7 values of total central face-on optical depth in B band τ_B^{f}, 8 inclinations i and 5 wavelengths. For the sampling in τ_B^{f} we chose the set of values 0.1, 0.3, 0.5, 1.0, 2.0, 4.0, 8.0, which range from extremely optically thin to moderately optically thick cases. For the sampling in inclination we used $\Delta \cos(i) = 0.1$, and $0 \leq (1 - \cos(i)) \leq 0.7$, which correspond to $i = 0, 26, 37, 46, 53, 60, 66, 73°$. The limit of 73° in i was imposed since standard methods to derive apparent exponential scalelength from observed images are no longer applicable for higher inclinations. The simulations were performed in the standard optical/NIR bands B, V, I, J, and K. We also used the corresponding intrinsic images of the stellar emissivity (as would be observed in the absence of dust).

3. Derivation of apparent disk scalelengths and central surface brightnesses

3.1. Formalism

When extracting apparent scalelengths, central surface brightnesses and axis ratios from observed (dust attenuated) images of galaxy disks, the common procedure is to fit the observed surface-brightness distribution with the brightness distribution

corresponding to the projection of an inclined thin axisymmetric exponential disk. This brightness distribution takes the form:

$$I_{\text{app}} = I_{\text{app}}^{\text{c}} \exp\left(-\frac{\sqrt{(y^2/Q_{\text{app}}^2) + x^2)}}{R_{\text{app}}}\right) \quad (4)$$

where $I_{\text{app}}^{\text{c}}$ is the apparent central surface brightness, R_{app} is the apparent exponential scalelength, and Q_{app} is the apparent axis ratio b/a of the inclined disk (equivalent to the cosine of the apparent inclination of the disk). The coordinate system is oriented such that galaxies have their major axis along the x-axis.

The strategy we adopt in this paper is to use the same fitting procedure as used to fit real observations to derive $I_{\text{app}}^{\text{c}}$, R_{app} and Q_{app} from our simulated dust attenuated disk images. These quantities can then be compared with the corresponding intrinsic quantities I_0^{c}, R_0, and Q_0, where I_0^{c} is the intrinsic face-on surface brightness, R_0 is the intrinsic exponential scalelength, and Q_0 is the intrinsic inclination of the disk. The intrinsic quantities are known as input to our simulations or can be derived from the simulated dustless face-on images: R_0 is equal to the value of the scalelength of the stellar emissivity $h_{\text{s}}^{\text{disk}}$, Q_0 is $\cos(i)$ for a simulation made with inclination i, and I_0^{c} is the brightness of the central pixel of the simulated dustless face-on image. The ratios $I_{\text{app}}^{\text{c}}/I_0^{\text{c}}$, R_{app}/R_0, and Q_{app}/Q_0 can then be used to quantify the discrepancy between intrinsic and perceived quantities arising from the presence of dust.

3.2. Technical procedure of the fit

The simulated disk images containing 700×1400 pixels and covering half a galaxy were first converted into full images of galaxies containing 1399×1400 pixels. The sky-value was zero by construction. The maximum of the light distribution was determined and was used as the centre of the disk fit.

The two-dimensional surface-brightness function from Eq. (4) was fitted to the brightness distribution of the simulated images following Möllenhoff & Heidt (2001). Fitting I_{app} to the two-dimensional surface-brightness distribution results in a nonlinear system of equations for the 3 free parameters $I_{\text{app}}^{\text{c}}$, R_{app} and Q_{app}. A Levenberg-Marquardt algorithm was used for the solution of this system (e.g. Bevington & Robinson 1992).

Several technical steps were necessary as prerequisites for the fit: The centre of the galaxy was determined in each image and the function from Eq. (4) was fitted to the whole image. Since there were 280 images to fit, a systematic procedure was necessary. We started in K with the face-on image and the lowest optical depth ($i = 0°$, $\tau_B^{\text{f}} = 0.1$). A rough guess for the start values of the parameters in the initial Levenberg-Marquardt fit was sufficient. The resulting parameters $I_{\text{app}}^{\text{c}}$, R_{app} and Q_{app} were used as start values for the next fits ($i = 0°$, $\tau_B^{\text{f}} = 0.3, 0.5, 1.0, 2.0, 4.0, 8.0$). Then the same procedure was repeated with the inclinations $i = 26°$ until $i = 73°$. Afterwards we proceeded in the same manner for the other filters J, I, V, B.

Figure 1 shows two examples of simulated disks and of residua after subtraction of our photometric fits to these simulated disks. For face-on galaxies the fit is perfect and the residuum is practically zero. For inclined galaxies the stronger forward scattering induces a relative brightening of the near side of the disk, leading to an asymmetry around the horizontal axis. Such an asymmetry is not considered by our fitting function, therefore the fit to the inclined galaxies will be imperfect.
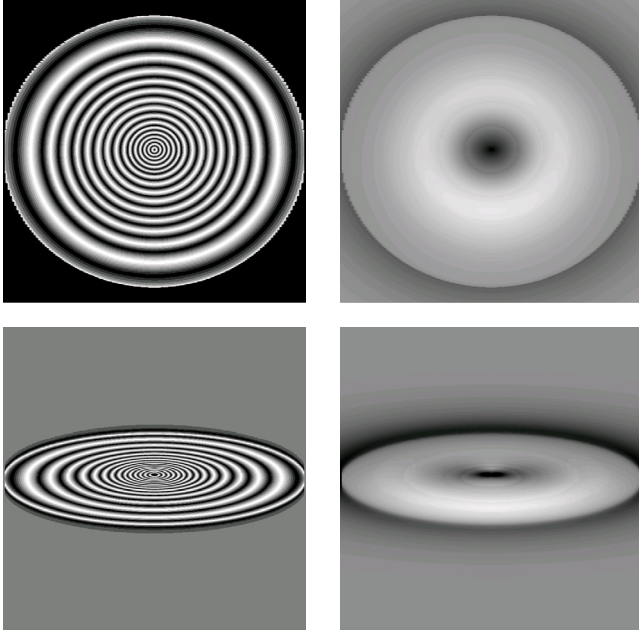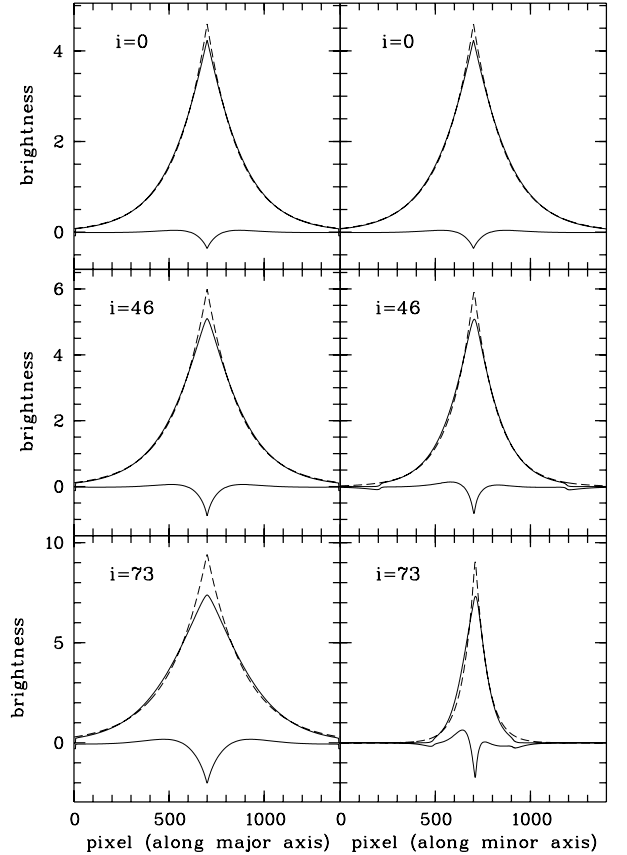
Fig. 1. *Top*: *B* image of the dusty disk model $i = 26°$, $\tau_B^f = 8.0$ (*left*) and residuum after subtraction of the photometric fit (*right*). *Bottom*: *B* image of the dusty disk model $i = 73°$, $\tau_B^f = 8.0$ (*left*) and residuum after subtraction of the photometric fit (*right*). For a better visibility an alternating intensity table for the disk models was chosen which produced the isophote-like images.

Fig. 2. Behaviour of two-dimensional fits and residua for simulations done in the *B* band, for $\tau_B^f = 1.0$, and for 3 different inclinations: $i = 0$ (*top*), $i = 46$ (*centre*), and $i = 73°$ (*bottom*). Each panel shows cuts parallel and perpendicular to the major axis, taken through the centres of the simulated galaxy (solid lines), of the fit (dashed lines), and of the residuum (solid lines at bottom).
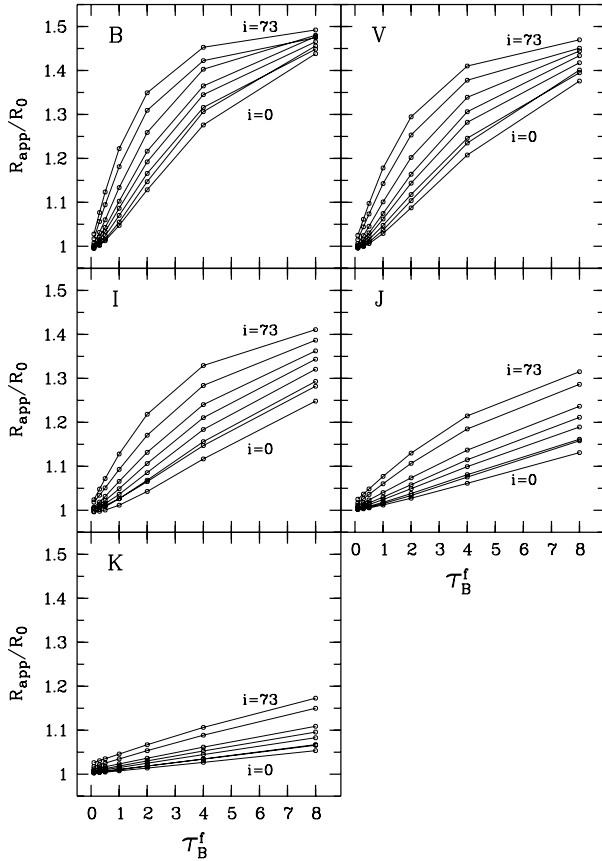
To show the details of the photometric fits and of the residua between the simulated disks and the fits, we plot in Fig. 2 cuts parallel and perpendicular to the major axis. This is shown for simulations done in the *B* band, for $\tau_B^f = 1.0$ and for three different inclinations, $i = 0, 46, 73°$. Due to the central opacity the disk models are somewhat rounder in the centre than the corresponding exponential fits. This effect is reflected in the central cusp of the residuum (solid bottom line) and increases with increasing inclination. Nevertheless the exponential fit is a good representation of the simulated brightness distribution. The above mentioned asymmetry due to dust scattering is especially prominent at high inclination in the cuts perpendicular to the major axis (bottom right panel of Fig. 2).

4. Results of the photometric fits

Tables 1 to 5 show the results of the fitting procedure for the *B*, *V*, *I*, *J*, and *K* bands. For each table the first two columns contain the input parameters inclination *i* and central face-on central optical depth in the *B* band τ_B^f and the last four columns contain the output parameters Q_{app}, R_{app}/R_0, I_{app}^c/I_0^c (as defined in Sect. 3.1) and ΔSB. $\Delta SB = -2.5 \log(F/F_0)$ is the ratio of the apparent average central surface brightness *F* to the intrinsic average central face-on surface brightness F_0, expressed in magnitudes. *F* is an average taken over an elliptical aperture[3] centred on the position of peak brightness in the simulated dusty image, with a semi-major axis of $R_{\mathrm{app}}/10$ and an axis ratio of $\cos(i)$. F_0 is an average taken over a circular aperture centred on the position of

peak brightness of the face-on dustless simulated image, with a radius $R_0/10$.

Here we should mention that the results given here are, as described in Sect. 3.2, obtained by fixing the coordinates of the centre of the fit to the position of maximum observed brightness. Other fitting procedures such as GIM2D (Simard 1998; Marleau & Simard 1999) or GALFIT (Peng et al. 2002) constrain the coordinates of the centre from the moments of the two-dimensional intensity distribution, which result in a small shift along the minor axis of the fitted centre for opaque high-inclination disks. The effect of this shift on the derivation of the central brightness is at most 3%. The effect on the derivation of the scalelength is negligible, since it depends only to second order on the shift.

In the following subsections we describe the general behaviour of the structural parameters listed in Tables 1–5 as a function of τ_B^f, *i* and wavelength.

4.1. Change of the exponential scalelengths

In Fig. 3 we show the dependence of R_{app}/R_0 on τ_B^f, for different inclinations and wavelengths. Because disks are always more attenuated in their central regions than in their outer regions, R_{app}/R_0 is always greater than unity and increases monotonically with τ_B^f. In some cases this increase is linear, whereas in others the increase flattens off towards higher values of τ_B^f. The linear behaviour happens when the disk is optically thin along the lines of sight towards most of the projected radii. As τ_B^f increases, an increasing area of the inner disk becomes optically

---

[3] We give the average surface brightness in an aperture (in addition to the surface brightness at the centre position of the fitted template) because in practice the brightness is blurred over a point spread function. Therefore it is useful to include a reference aperture which is larger than typical point spread functions, but smaller than the scalelength of the disk.

Fig. 3. The ratio of the apparent to intrinsic scalelengths R_{app}/R_0 versus τ_B^f, for $i = 0, 26, 37, 46, 53, 60, 66, 73°$, and for the wavebands B, V, I, J and K.

Fig. 4. The ratio of the apparent to intrinsic scalelengths R_{app}/R_0 versus $1 - \cos(i)$, for $\tau_B^f = 0.1, 0.3, 0.5, 1.0, 2.0, 4.0, 8.0$, and for the wavebands B, V, I, J, and K.

thick, producing a slowing-down in the increase with τ_B^f, until an asymptote is approached when the disk becomes optically thick along the lines of sight over the whole extent of the disk. At longer wavelengths, e.g. in the K band, such an asymptote is never reached and the behaviour of the curves remains in the linear regime, since even at the highest τ_B^f and inclinations considered, the disk remains optically thin along most of the lines of sight. By contrast, at the shorter wavelengths, for instance in the B band, the asymptote is approached for high τ_B^f and inclinations, as the disk becomes optically thick along most of the lines of sight. Furthermore, at these wavelengths the curves enter the non-linear regime at all inclinations, since some part of the disk is always optically thick along the line of sight. At intermediate wavelengths, such as in the I band, the variation with τ_B^f remains in the linear regime at lower inclinations, and only at high inclination is a non-linear behaviour seen, though without getting near the asymptote. Another consequence of the existence of the asymptote is that the curves for different inclinations tend to bunch together at high τ_B^f and shorter wavelengths, as the asymptote is approached. Thus, in B, V and I bands, the highest spread between the curves at different inclinations is reached at intermediate τ_B^f, since, by necessity, the curves must also be bunched together at low τ_B^f. In K band the curves never enter the non-linear regime so the maximum spread happens at the highest τ_B^f.

In Fig. 4 we plot the same information as in Fig. 3, but as the variation of R_{app}/R_0 with inclination, for different τ_B^f and wavelengths. The curves appear flat when the disk is either predominantly optically thin at all inclinations (for example in K band
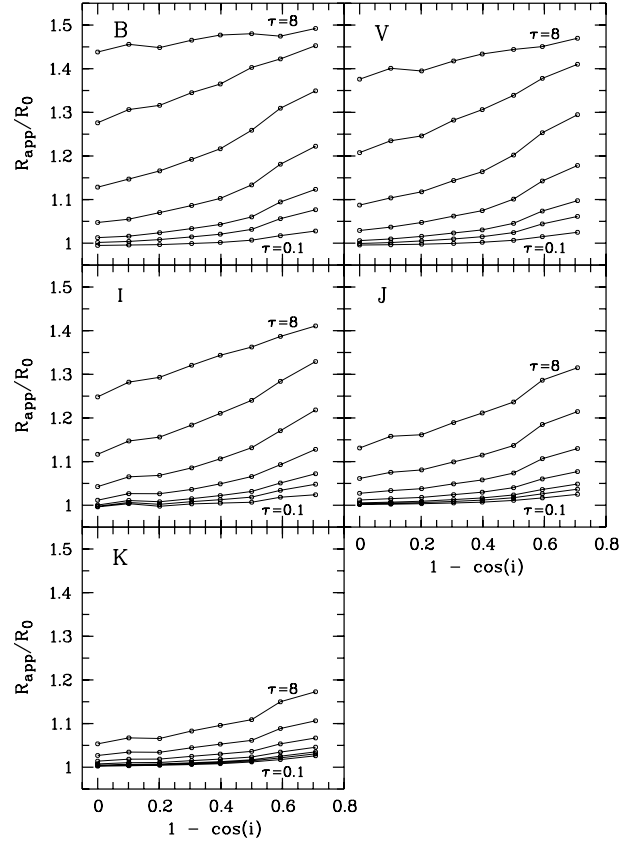
at $\tau_B^f < 2$, where R_{app}/R_0 is close to unity) or when the disk is predominantly optically thick at all inclinations (for example in B band at $\tau_B^f = 8$, where R_{app}/R_0 approaches the asymptote of 1.5).

In Fig. 5 we plot R_{app}/R_0 versus wavelength, for different τ_B^f and inclinations. The variation with wavelength also shows a transition between a linear behaviour in an optically thin regime (for $\tau_B^f < 0.5$) and a non-linear approach to an asymptote at $\tau_B^f = 8$.

In order to see what is the relative change in the scalelength between different wavelengths just due to the effect of dust, one can look at the variation of the quantity $\frac{R_{app}(\lambda_1)}{R_{app}(\lambda_2)} \times \frac{R_0(\lambda_2)}{R_0(\lambda_1)}$ with τ_B^f. As an example, we plot in Fig. 6 this quantity for the wavelengths B and I. At all inclinations, the curves show a similar basic shape. The curves rise steeply at low τ_B^f, reach a maximum and then decline slowly. This behaviour is compressed over a smaller range of τ_B^f for higher inclinations. Because of this, $\frac{R_{app}(B)}{R_{app}(I)} \times \frac{R_0(I)}{R_0(B)}$ increases with inclination at low τ_B^f, but decreases with inclination at high τ_B^f, with the curves crossing at intermediate τ_B^f. In other words, for a low τ_B^f, in order to convert the ratio between the apparent scalelength in B and I to the corresponding intrinsic ratio, one needs to apply a correction factor which is larger for high inclinations than for low inclinations, whereas at high τ_B^f the opposite is true. An interesting feature of these curves is that they are relatively flat for $\tau_B^f > 2$.
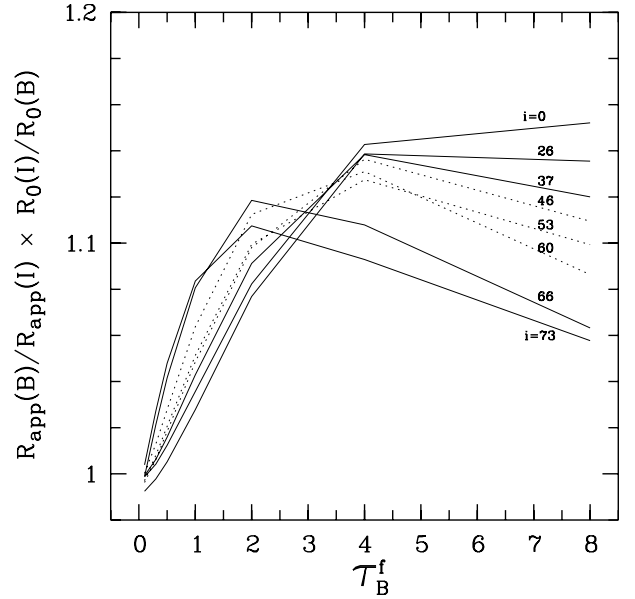
Simulations of the observed ratios of scalelength in B and I as a function of inclination and τ_B^f have also been performed by
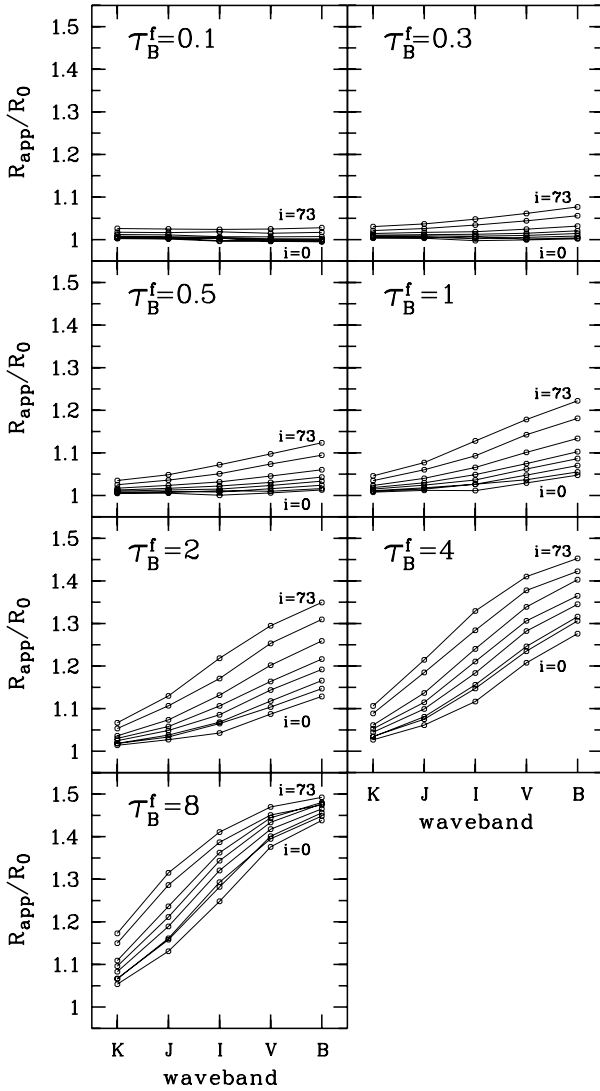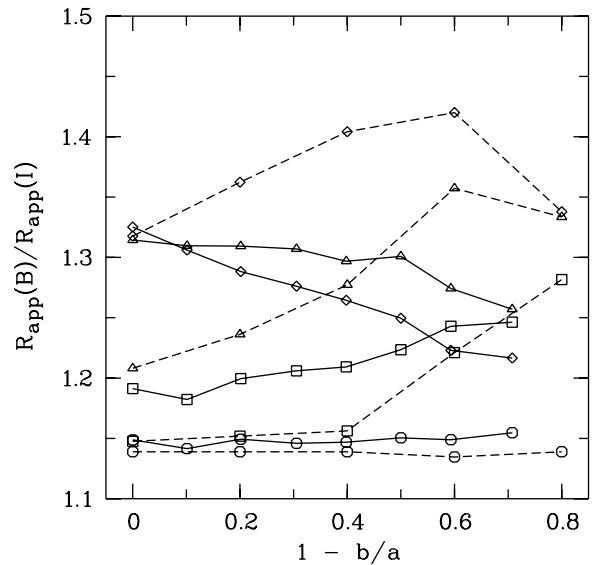
Fig. 5. The ratio of the apparent to intrinsic scalelengths R_{app}/R_0 versus waveband, for $i = 0, 26, 37, 46, 53, 60, 66, 73°$, and for $\tau_B^f = 0.1, 0.3, 0.5, 1.0, 2.0, 4.0, 8.0$.

Fig. 6. The change in the ratio of the scalelengths in B and I bands due to the effects of dust, plotted as $\frac{R_{app}(B)}{R_{app}(I)} \times \frac{R_0(I)}{R_0(B)}$ versus τ_B^f. Different curves are plotted for a range of inclinations from $i = 0$ to $i = 73$. The curves for intermediate inclinations ($i = 46$, $i = 53$ and $i = 60$) are plotted with dotted lines for clarity.

Fig. 7. Comparison between the apparent ratios of scalelength in B and I predicted by our work (solid lines) and by the work of Cunow et al. (2001) (dashed lines). The curves are for $\tau_B^f = 0.1$, 1, 4 and 8 (interpolated in the case of the Cunow curves). The pairwise corresponding curves are marked by 4 different symbols.

Cunow et al. (2001). The closest comparison possible is that with model (k) of Cunow, which differs from our model only through the absence of the dust disk associated with the young stellar population. In Fig. 7 we have plotted the ratios of apparent scalelength in B and I as a function of apparent ellipticity $(1 - b/a)$ for both our model and the model from Fig. 7 of Cunow et al. (2001), where the ratios from Cunow have been interpolated to match the opacities given in our tables. Overall the curves of Cunow behave as if their model is more optically thin for the same τ_B^f, which is the opposite behaviour one would expect from the differences in the geometrical distributions between the models. However the procedure to derive scalelength followed by Cunow et al. only uses data from the outer parts of the disk having a linear profile, whereas our method uses data from the whole disk. This obviously biases the results from Cunow towards more optically thin solutions and this effect dominates over the differences induced by the different geometrical distributions.

Another work on predicting apparent scalelength ratios between B and I is that of Byun et al. (1994). These results are very similar to those of Cunow et al. (2001) (see Fig. 8 of

Cunow et al.), which may reflect the fact that Byun et al. also use extrapolation from the outer disk in deriving photometric parameters.

4.2. Change of the central surface brightness

In Fig. 8 we show the dependence of ΔSB on τ_B^f, for different inclinations and wavelengths. An interesting feature of these curves is that they pass through both positive and negative values of ΔSB: the centre of the disk can appear either dimmer
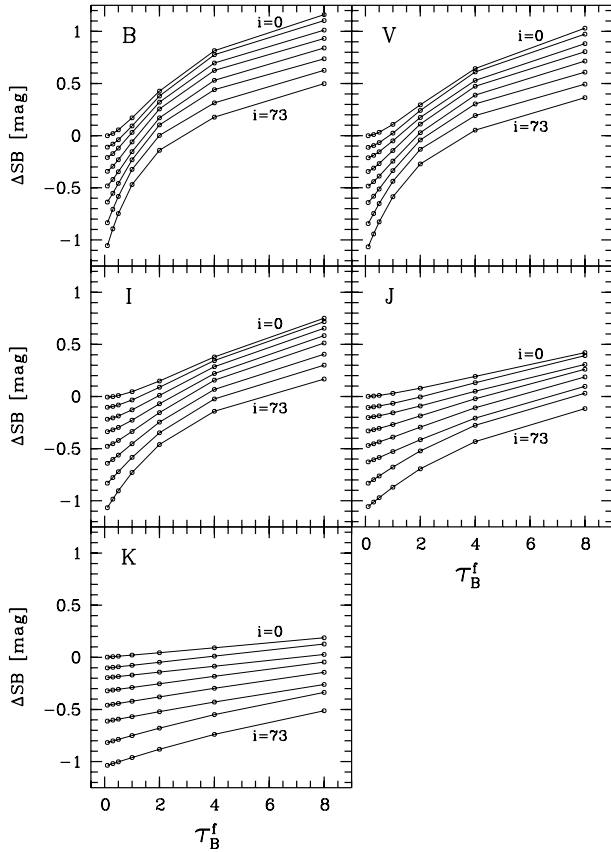
Fig. 8. The ratio of the apparent average central surface brightness to the intrinsic average central face-on surface brightness expressed in magnitudes, ΔSB, versus τ_B^f, for $i = 0, 26, 37, 46, 53, 60, 66, 73°$, and for the wavebands B, V, I, J, and K.

or brighter than the face-on dustless disk. This is because the projected surface density of stars visible along the line of sight can be either greater or smaller than the surface density of stars seen towards the centre of a face-on dustless disk. The projected surface density of stars can be increased by viewing the disk at higher inclinations and can be decreased by attenuating the stellar light with dust. In the K band the central part of the disk appears brighter than the centre of the face-on dustless disk at almost all inclinations and τ_B^f, because the line of sight through the centre is almost always transparent. On the contrary, in the B band the opposite is true, since the line of sight through the centre is almost always opaque.

The form of the curves in Fig. 8 can be explained in terms of the two competing factors viewing angle and opacity: the brightening of the SB_{app}^c with increasing inclination and the dimming of the SB_{app}^c with increasing τ_B^f. The former effect is independent of wavelength, since the line of sight of stars is always the same for a certain inclination[4] This can be seen from the wavelength independence of the spread in ΔSB from 0 to -1 mag for $\tau_B^f = 0$. The latter effect (the dimming due to opacity) is strongly dependent on wavelength, since, for a certain τ_B^f, the depth into which stars can be seen along the line of sight decreases with

---

[4] Formally there is a very small dependence on wavelength due to the fact that the scalelength of the stars varies with wavelength in our model. In practice, however, this effect is negligible over the range of inclinations considered here and cannot be seen in the plot.

decreasing wavelength. The dimming of SB_{app}^c with increasing τ_B^f is almost negligible in the K band at inclinations close to face-on, when the line of sight through the centre is almost transparent. On the contrary, in the B band this effect becomes strong at all inclinations.

Another feature of these curves is the transition between a linear dependence of ΔSB on τ_B^f when the lines of sight through the centre are optically thin (e.g. in the K band at all inclinations), to a non-linear regime for optically thick lines of sight (e.g. in the B band at all inclinations). At intermediate wavelengths (e.g. in the J band) one sees a transition between these two regimes: the upper curves (close to face-on) are in the linear regime, whereas the lower curves (high inclinations) are non-linear.

For a given (non-zero) τ_B^f, the dispersion between the curves in Fig. 8 for low and high inclinations varies systematically with wavelength. For the case of $\tau_B^f = 4$ one can see that the dispersion has a maximum in the K band, then it decreases towards I band, after which it increases again towards B band. At first glance this behaviour is not very intuitive. If the stars and dust had an identical distribution, then one would expect a monotonic decrease in dispersion when moving from transparent central disks to opaque central disks, until the lines of sight would become completely opaque at all inclinations and the dispersion would tend to zero (since the brightness of an optically thick body is independent of the viewing angle). The fact that the behaviour is more complex than this is a consequence of the non-identical distribution of stars and dust in the vertical direction. In our model the stars and dust are distributed in exponential disks, with the stars having scaleheights larger than those of the dust. As already remarked by Disney et al. (1989), "even in a highly obscured galaxy, the upper layers of unobscured stars will apparently increase its mean surface brightness as it is inclined, mimicking the behaviour of an optically thin system". Thus, at the extreme of very high optical depth one approaches the same dispersion as for the very low optical depth, since the variation in the surface brightness between low and high inclination is only produced by the stars above the (exponential) dust layer. At intermediate optical depths the dispersion over inclination is lower, because a larger fraction of this dispersion comes from stars well mixed with the dust which have a smaller variation in the surface brightness between low and high inclination. In our model, there will always be an increase in the surface brightness with increasing inclination, even for optically thick disks. This can be seen even better in Fig. 9, where we plot the same information as in Fig. 8, but as the variation of ΔSB with inclination, for different τ_B^f and wavelengths. We also plotted the variation ΔSB with wavelength (Fig. 10), for different τ_B^f and inclinations, to better capture the transition between the almost independence of ΔSB on wavelength at low τ_B^f to a strong dependence on wavelength at high τ_B^f. In order to see what is the change in the central colour of the disk due to dust, one can look at the variation of $\Delta SB(\lambda_1) - \Delta SB(\lambda_2)$ with τ_B^f. As for the analogous plot for the variation of scalelength, we plot in Fig. 11 this quantity for the wavebands B and I, $\Delta SB(B) - \Delta SB(I)$, which is equivalent to a plot of $SB(B) - SB(I)$ shifted by a constant value, such that the curves go through the origin. These curves, therefore, give the colour correction that needs to be applied to correct apparent colour to intrinsic colour at the centre of the disk. The curves show the same qualitative behaviour as those for the relative change in scalelength, namely that they rise steeply at low τ_B^f, reach a maximum and then decline slowly. We note again the relatively flat behaviour of the curves for $\tau_B^f > 2$.
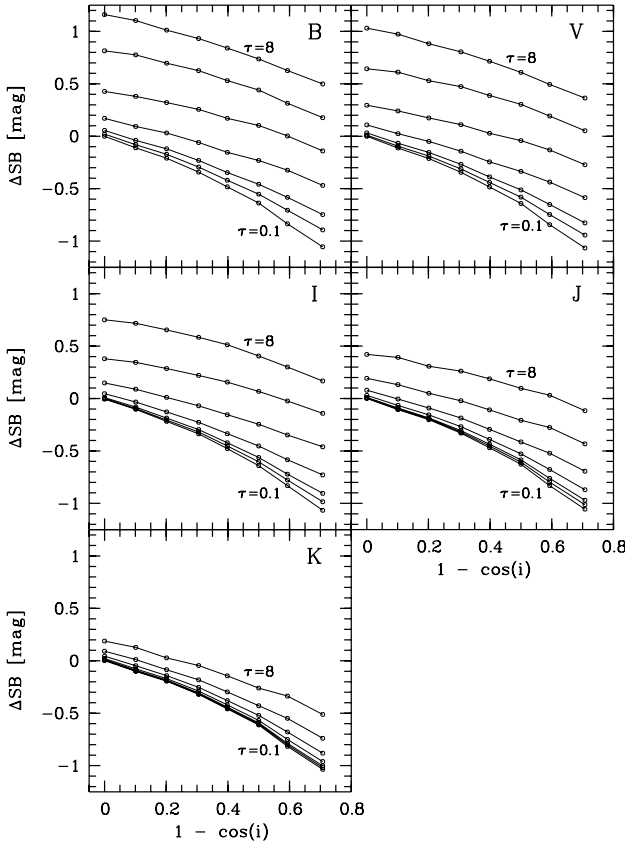
Fig. 9. The ratio of the apparent average central surface brightness to the intrinsic average central face-on surface brightness expressed in magnitudes, ΔSB, versus $1 - \cos{(i)}$, for $\tau_B^f = 0.1, 0.3, 0.5, 1.0, 2.0, 4.0, 8.0$ and for the wavebands B, V, I, J, and K.
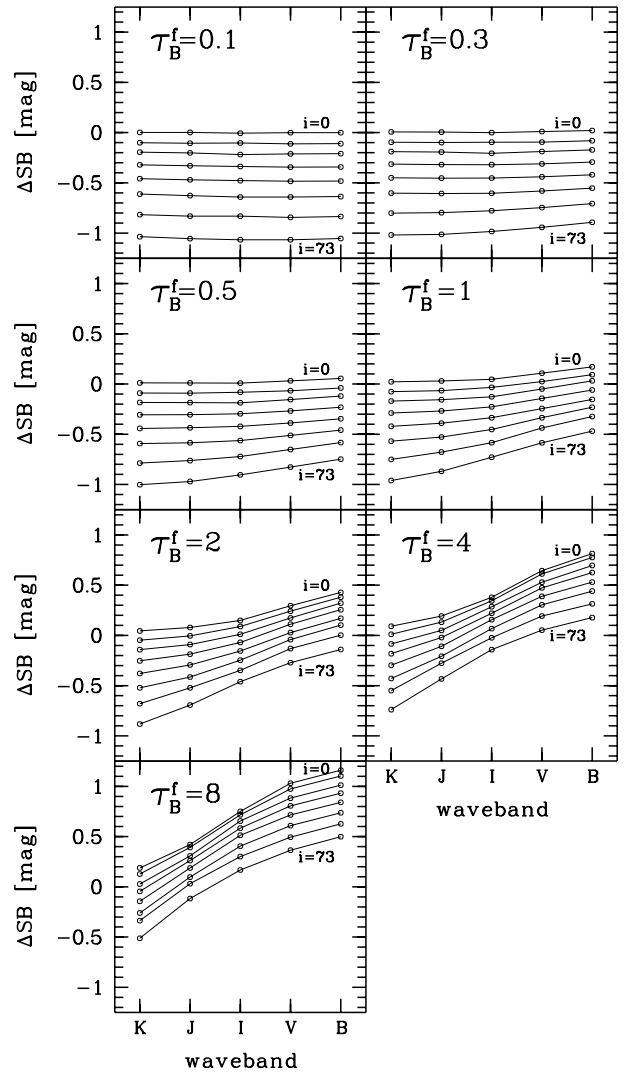

Fig. 10. The ratio of the apparent average central surface brightness to the intrinsic average central face-on surface brightness expressed in magnitudes, ΔSB, versus waveband, for $i = 0, 26, 37, 46, 53, 60, 66, 73°$, and for $\tau_B^f = 0.1, 0.3, 0.5, 1.0, 2.0, 4.0, 8.0$.

4.3. Change of the axis ratios

In Fig. 12 we show the dependence of the ratio of the apparent to the intrinsic axis ratio, Q_{app}/Q_0 on τ_B^f, for different inclinations and wavelengths. One can see that this ratio can be either greater or less than one, which means that the galaxy can appear less or more inclined than it is in reality. In other words the galaxy can appear rounder or flatter than the shape of an infinitely thin dustless disk at the true inclination of the galaxy. This behaviour is attributed to two effects that act in the opposite sense. Firstly, the vertical distribution of stars makes the galaxy appear rounder than an infinitely thin dustless disk. Secondly, the presence of dust makes the galaxy appear flatter than an infinitely thin dustless disk. The first effect is obvious, but the second needs some explaining. As one increases the line of sight optical depth, either by increasing the inclination or the τ_B^f, the observed light becomes dominated by photons originating from an increasingly thin stellar layer on the side of the dust disk nearest to the observer, due to absorption by dust of photons originating from below this layer.

The effect of the vertical distribution of stars is best seen by looking at the inclination dependence of Q_{app}/Q_0 for τ_B^f close to zero. For example in the K band, Q_{app}/Q_0 increases monotonically with inclination up to ~1.13 for $i = 73°$.

The effect of opacity is more complex. One feature is the decrease of Q_{app}/Q_0 with increasing τ_B^f, for all inclinations and wavelengths. This effect is weak in the K band where opacity is small, and is strong in the B band where opacity is large. A further aspect of the effect of dust is that at high opacity, and

except for inclinations near to edge-on, the dependence of Q_{app}/Q_0 on inclination is the opposite of that predicted by the model at low opacity. Thus, in B-band at $\tau_B^f = 8$, the general trend is for Q_{app}/Q_0 to decrease with increasing inclination[5] over the range $i = 0$ to $i = 66$, as one progressively sees a thinner and thinner layer of stars above the dust layer, making the galaxy appear flatter with increasing inclination. Suddenly, at $i = 73$, this trend is reversed, as one starts to see stars both above and below the dust layer, and a big step is made to a rounder shape. The different behaviour of Q_{app}/Q_0 on inclination at low and high $\tau_B^f = 8$ means that the curves cross at intermediate τ_B^f.

5. Discussion

Having established the dependence on inclination, face-on opacity and wavelength of the corrections needed to convert the apparent photometric parameters scalelength, central surface brightness and axis ratios into the corresponding intrinsic

---

[5] Within the numerical noise induced by the finite numbers of directions for which scattered light is calculated.
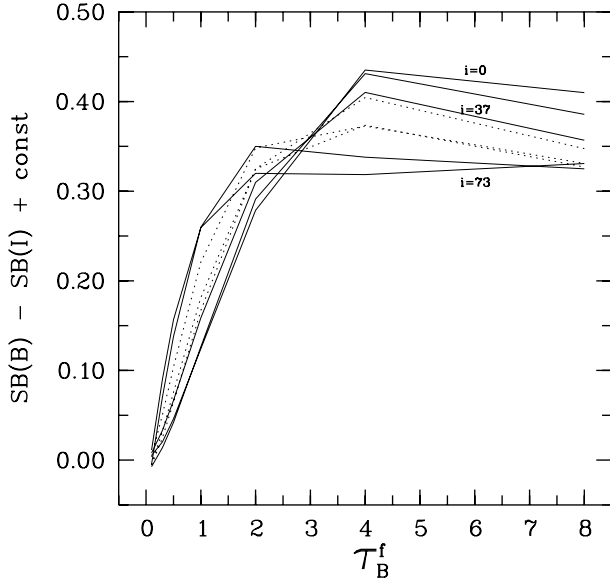
Fig. 11. The change in the $B - I$ central colour due to the effects of dust, plotted as $\Delta SB(B) - \Delta SB(I) + \mathrm{const.}$ versus τ_B^f. Different curves are plotted for a range of inclinations from $i = 0$ to $i = 73$. The curves for intermediate inclinations ($i = 46$, $i = 53$ and $i = 60$) are plotted with dotted lines for clarity.

Fig. 12. The ratio of the apparent to intrinsic axis ratio Q_{app}/Q_0 versus τ_B^f, for $i = 0, 37, 53, 66, 73°$ and for the wavebands B, V, I, J, and K.

quantities, we can now discuss the implications of these findings. But before doing this, we caution that the corrections given in this paper are valid only for disk-dominated galaxies. In reality, many galaxies have prominent bulges and therefore the apparent photometric parameters of the disk (including scalelength, central surface brightness and total magnitudes) have to be found in a simultaneous fit of geometrical functions for the bulge and the disk. However, the apparent photometric parameters derived from this bulge-to-disk decomposition will be a function of both opacity and bulge-to-disk ratio. In other words, the apparent scalelength and central surface brightness that one derives for a disk galaxy with a given opacity and inclination in the presence of a bulge will in general be different from the apparent scalelength that one derives for the same disk (with the same opacity and inclination) without a bulge. Therefore one should restrict the analysis to galaxies having small bulges, where such effects can be ignored.

One should also caution that the corrections for dust given in this paper are calculated assuming a small wavelength dependence of the ratio of the intrinsic scalelength of the stars to that of the dust, as specified in Tuffs et al. (2004). Thus, strictly speaking, the tabulated corrections are valid only for this geometry. In practice, however, these corrections can be used also for systems having a different variation in the ratio of the intrinsic scalelengths. Comparison between Figs. 7b and h from Cunow et al. (2001) show that, if one were to make an error of 25% in the assumed intrinsic scalelength of stars relative to the dust, the corresponding error in the effect of dust would be at most a few percent for typical opacities and inclinations less than 70°. Only for $\tau_B^f > 7$ and inclination greater than 70° does the error exceed 10%.

After these words of caution we can now examine the impact of these new results on our ability to derive quantities of astrophysical interest from optical observations of disk-dominated galaxies. In principle, if one knew the face-on opacity, one could use the correction factors to analyse the intrinsic properties of galaxies on an object to object basis. In practice,
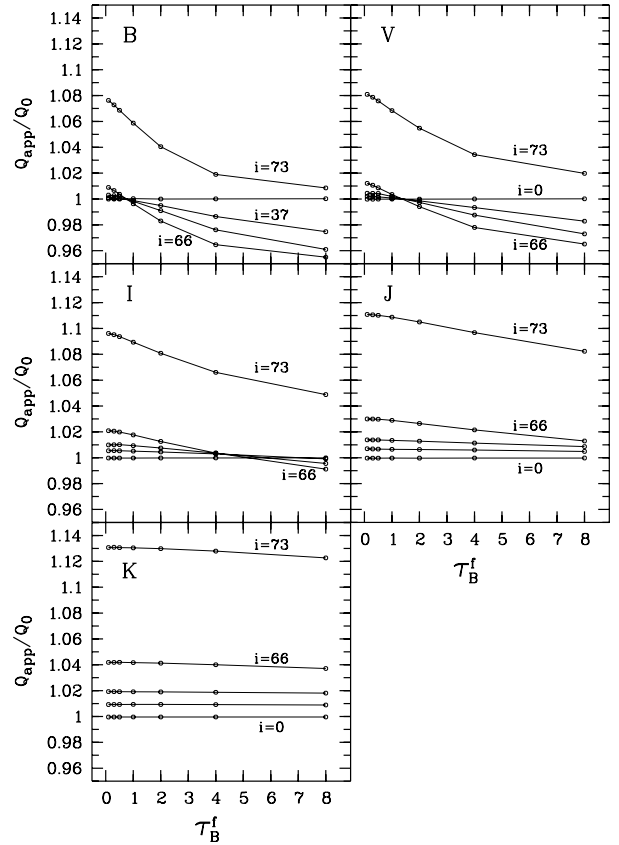
however, the face-on opacity of an individual galaxy can only be reliably determined by self-consistently modelling its combined UV/optical/FIR/submm output, which is at present only rarely possible, since the vast majority of galaxies has not yet been measured in the FIR/submm regime. For large statistical samples, though, one can derive a characteristic value for the face-on opacity of a population of systems from the optical measurements themselves by analysing the inclination dependence of the photometric parameters described here.

One can also use our tabulated corrections for the investigation of astrophysical effects for which, although the absolute effect of dust is non-negligible, the predicted variation over a likely range in opacity is relatively small, such that an exact knowledge of opacity is not needed. An example is the variation of the scalelength between B and I due to dust, which is small, provided that $\tau_B^f > 2$ (galaxies are not too optically thin)[6]. Indeed, inspection of Fig. 6 shows that for a galaxy at a typical inclination of 37° and having any $\tau_B^f > 2$, the effect of dust is to increase the scalelength in B relative to that in I by a factor of 1.12 ± 0.02. The scatter in this ratio is so small that one can compare the intrinsic scalelength of the stellar populations in B and I by simply applying a single correction factor for dust for any spiral galaxy at this inclination. Similarly, other correction factors can be derived from our tables for other inclinations and other waveband combinations.

Correspondingly, one can also compare the surface brightnesses between B and I to get information about the intrinsic

---

[6] In our detailed SED modelling of individual galaxies given in Papers I and II we showed that this range in opacity is quite likely to characterise spiral galaxies.

colour of the central and most dust affected regions of the disks, even without detailed knowledge of τ_B^f. Inspection of Fig. 11 shows that for a galaxy at an inclination of 37° and for $\tau_B^f > 2$, the change in $B - I$ central colour due to dust is 0.36 ± 0.05 mag. Again, the scatter in the central colour is small enough that one can look at the intrinsic central colour between B and I by simply applying a single correction factor for dust for any spiral galaxy at this inclination.

Lack of knowledge of opacity may be somewhat more problematic when one attempts to compare the properties of dusty galaxies in the local and distant universe at a fixed restwavelength. When studying the evolution of disk sizes with redshift (e.g. by comparing the scalelength of low ($z \sim 0$) and high ($z \sim 1$) redshifted galaxies at a common restwavelength) one must correct for the increase in the apparent disk scalelength with increasing redshift, stemming from the expected increase in opacity. If, for example, the opacity increased from 4 at $z = 0$ to 8 or more at $z = 1$, the apparent scalelength in the B band of a galaxy seen at $i = 37°$ would increase by a factor of at least 1.10 due to dust. This factor would rise to at least 1.24 for an increase in opacity from 2 to 8 or more. The increase in the apparent scalelength with increasing redshift due to the effect of dust goes in the opposite direction to the predicted evolution in intrinsic disk size, and in general would need to be taken into account in quantitative analyses. Ultimately one would need to refine the technique to take into account the possible evolution of the dust/star geometry[7] when making corrections for high-redshifted galaxies. This will become possible when spatially resolved dust emission data from the rest-frame far-infrared is available for such systems, thereby permitting an analysis of the star/dust geometry to be performed analogous to that performed for local universe galaxies.

Our tabulated corrections for dust will also allow the analysis of the correlation between the central face-on surface brightness versus scalelength, as investigated by Graham (2001) in the K band where the galaxies are optically thin, to be extended to the shorter wavebands where the galaxies may be optically thick. As a by-product of such an investigation, we note that one could obtain a statistical determination of τ_B^f from the inclination dependence of both central surface-brightness and scalelength. As previously cautioned, however, this analysis has for the moment to be restricted to disk-dominated galaxies.

6. Application to local universe disk galaxies

As mentioned in the introduction, one of the motivations of this work is to quantify the change in the intrinsic scalelength of different stellar populations in local universe disk galaxies. Here we give an example of the application of our model to such an investigation. For this we used published apparent disk scalelengths in B and I, restricting the data to galaxies which have measured bulge-to-disk ratios of less than 0.2. There are two reasons for this selection criterion. Firstly, as mentioned in the discussion, one needs to restrict the analysis to disks with small bulges, since the apparent scalelength derived for dusty disks with large bulges will diverge from the apparent scalelength of pure dusty disks. Secondly, for systems with small bulges MacArthur et al. (2003) showed that results from one-dimensional photometry are equivalent to those derived from two-dimensional fits (as required by this work). The resulting sample is comprised of 61 galaxies
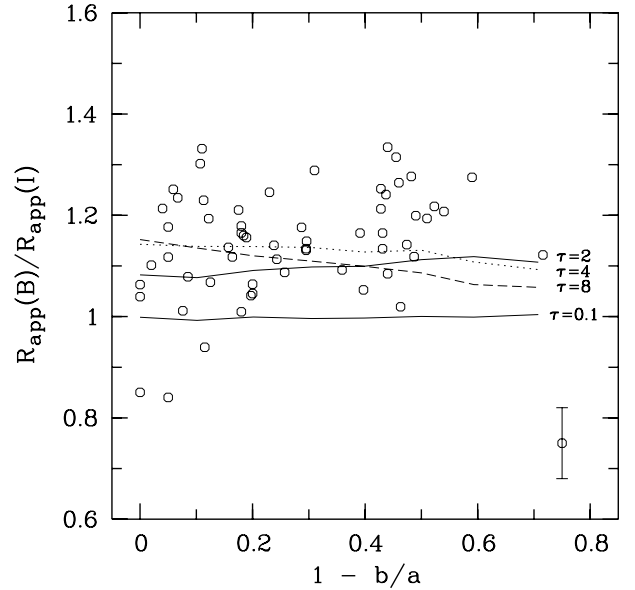
Fig. 13. Observed scalelength ratios between B and I, $\dfrac{R_{\mathrm{app}}(B)}{R_{\mathrm{app}}(I)}$, versus observed axis ratios $1 - b/a$. The lines represent the model predictions for the same relation due only to the effect of dust, which is equivalent to the prediction of apparent scalelength ratios for dusty disks having the same intrinsic scalelength in B and I. The lines correspond to $\tau_B^f = 0.1, 2, 4, 8$. A typical error bar of 7% is plotted in the lower right hand corner.

taken from Möllenhoff (2004), MacArthur et al. (2003), Prieto et al. (2001) and Pompei & Natali (1997). Since MacArthur et al. had measurements in $B \, V \, R \, H$, their R band scalelengths were converted to I band scalelengths by multiplying them by a factor of 0.981. This factor was obtained by linearly interpolating between the average scalelength in R and H, as given in Table 3 of MacArthur et al. Despite our selection of disk-dominated galaxies and the known tendency of such systems to preferentially populate the intermediate- and low-mass end of the mass distribution of nearby, late-type galaxies (e.g. Pierini & Tuffs 1999), the galaxies used in this sample are all bright spiral galaxies with absolute magnitudes $M_V = -19.2$ to -22.3. Thus they have geometries of stars and dust appropriate to giant spirals, which are well described by our model.

In Fig. 13 we plot observed scalelength ratios between B and I, $\dfrac{R_{\mathrm{app}}(B)}{R_{\mathrm{app}}(I)}$, versus axis ratios $1 - b/a$. All but three of the 61 data points lie above unity, which means that almost all galaxies have apparent scalelengths which are larger in B than in I. The data also show a scatter, which is consistent with the random errors estimated for the measurements[8]. The mean and the standard deviation in $R_{\mathrm{app}}(B)/R_{\mathrm{app}}(I)$ is 1.156 and 0.094, respectively. In order to see whether these observed values can be accounted for by the effect of dust alone, we compare them with model predictions for $\tau_B^f > 2$ (see Fig. 13) which is a reasonable range in τ_B^f to expect for disk galaxies. For each of the model predictions we calculated the corresponding ratio of intrinsic scalelengths at B and I which best fit the data by shifting the lines vertically in the figure until an equal number of data points appeared above and below the line. This process yielded average ratios of

---

[7] For example, depending on the assumed star-formation history, it may be necessary to invoke different star/dust geometries to explain the observed colours of distant disk galaxies (Pierini et al. 2005).

[8] The errors of a single scalelength determination were estimated to be ~5% in Möllenhoff, ~3% in Cunow and ~5% in MacArthur et al. Thus the error of the quotients in Fig. 13 can be estimated to be ~7%. A corresponding error bar is plotted there.

intrinsic scalelengths of 1.057, 1.019 and 1.037, for $\tau_B^f = 2, 4, 8$, respectively, and an overall range ($\pm 1\sigma$ for the sample) of intrinsic scalelength ratios from 0.93 to 1.15. Because the deviation from unity of the averaged ratios is so much less than the spread in the individual data points, we conclude that, on average, and within the available statistics, there is almost no systematic increase in the intrinsic scalelength with decreasing wavelength and that the observed predominance of galaxies with ratios of apparent scalelengths greater than unity is mainly due to the effects of dust. The data would only admit a small variation of the intrinsic stellar scalelength between B and I (less than 1.15) if $\tau_B^f < 2$. However combined analysis of the UV/optical and FIR/submm have generally yielded $\tau_B^f < 2$ (Bianchi et al. 2000b; Papers I, II; Misiriotis et al. 2004; Meijerink et al. 2005).

Much bigger statistical samples will be needed to measure systematic trends in intrinsic scalelengths with wavelength, if they exist. Finally we note that the scatter in the observed ratio of scalelengths between B and I (with $\sigma = 0.094$) is comparable to the estimated errors in this quantity for individual galaxies and can therefore primarily be ascribed to measurement errors.

Our conclusion that dust is mainly responsible for the larger scalelength observed in the B band compared to I band can be contrasted with the results from Cunow (2001, 2004), who deduced that dust alone was not sufficient to explain this effect. Here we note that the different conclusions can primarily be attributed to differences in the data rather than differences in the model. In fact, as noted by Cunow (2004), her data for normal galaxies, both in terms of the absolute values of the scalelength ratios and the variation of these ratios with inclination, cannot be fitted by any model. As shown in Fig. 13, our data is reasonably well fitted by our model in both these respects.

Another study in the literature that has addressed the wavelength dependence of scalelength (this time between B and K bands) is that of Peletier et al. (1994). Here again, on average, the scalelength ratios have much larger values than in our sample, even taken into account the different wavelength used. Although Peletier et al. interpreted their results as being due to the effect of dust on the apparent scalelengths, such large effects are not predicted by any dust model. Bearing in mind the inclusion of galaxies with bulges in the sample of Peletier et al., such effects are, in our view, more likely to be produced by the effect of dust on the bulge-disk decomposition itself. This is because the use of simple templates for dustless bulge and disk in bulge-disk decomposition would lead to systematic bias in the derived photometric parameters, including apparent disk scalelength.

7. Conclusions and summary

We have fitted the simulated images of dusty disk galaxies presented in Paper III with a template brightness distribution corresponding to an inclined infinitely thin dustless exponential disk to obtain apparent scalelengths, central surface-brightness distributions and axis ratios. These are the apparent photometric quantities that an observer would extract from observed images of galaxies. Using the prior knowledge of the corresponding intrinsic quantities input in the simulations, we were able to derive the correction factors (listed in Tables 1−5 of this paper) for the conversion of the apparent to intrinsic quantities due to dust, as a function of inclination i, central face-on optical depth in B band τ_B^f, and wavelength.

The apparent to intrinsic scalelength ratio is always greater than unity and can vary up to 50%. The apparent to intrinsic central surface-brightness ratio expressed in magnitudes can be either positive or negative, depending on whether the dimming due to dust is more or less important than the brightening due to the increase in the column density of stars induced by inclining the disk. This ratio can change up to 1.5 mag due to the effect of dust. The ratio of the apparent to intrinsic axis ratio is not strongly affected by dust, but has an opposite dependence on inclination according to whether the lines of sight through the disk are predominantly optically thin or optically thick. In the former case the vertical distribution of stars makes the galaxy appear progressively rounder with increasing inclination than an infinitely thin disk, whereas in the latter case the opposite trend is seen, because an increasing proportion of the observed light originates from a thin layer of stars above the dust.

Assuming that the basic geometry of dust and stars in local universe spiral galaxies also applies for higher redshift spiral galaxies, our tabulated corrections can be used to correct for the increase in the apparent disk scalelength with increasing redshift due to the expected increase in opacity. This will allow the intrinsic evolution of disk sizes with cosmological epoch to be investigated. As an example, we show that for a possible variation in opacity between 2 at $z = 0$ to 8 or more at $z = 1$, the apparent scalelength in the B band of a galaxy seen at $i = 37°$ would increase by a factor of at least 1.24 due to dust.

We used our model to analyse the distribution of observed scalelength ratios between B and I for a sample of disk-dominated spiral galaxies. We found that the predominance of galaxies with larger apparent scalelength in B than in I is primarily due to the effects of dust.

References

Barden, M., Rix, H.-W., Somerville, R. S., Bell, E. F., Häußler, B., et al. 2005, ApJ, 635, 959
Bevington, P. R., & Robinson, D. K. 1992, Data reduction and error analysis for the physical sciences, 2nd ed. (New York: McGraw-Hill)
Bianchi, S., Ferrara, A., Davies, J. I., & Alton, P. B. 2000a, MNRAS, 311, 601
Bianchi, S., Davies, J. I., & Alton, P. B. 2000b, A&A, 359, 65
Byun, Y. I., Freeman, K. C., & Kylafis, N. D. 1994, ApJ, 432, 114
Cunow, B. 1998, A&AS, 129, 593
Cunow, B. 2001, MNRAS, 323, 130
Cunow, B. 2004, MNRAS, 353, 477
Dalcanton, J. J., Yoachim, P., & Bernstein, R. A. 2004, ApJ, 608, 189
de Grijs, R. 1998, MNRAS, 299, 595
de Jong, R. 1996a, A&A, 313, 45
de Jong, R. 1996b, A&AS, 118, 557
Disney, M., Davies, J., & Phillipps, S. 1989, MNRAS, 239, 939
Dwek, E. 1998, ApJ, 501, 643
Elmegreen, D. M., & Elmegreen, B. G. 1984, ApJS, 54, 127
Evans, R. 1994, MNRAS, 266, 511
Graham, A. 2001, MNRAS, 326, 543
Haas, M., Lemke, D., Stickel, M., et al. 1998, A&A, 338, L33
Hippelein, H., Haas, M., Tuffs, R. J., et al. 2003, A&A, 407, 137
Kuchinski, L. E., Terndrup, D. M., Gordon, K. D., & Witt, A. N. 1998, AJ, 115, 1438
Kylafis, N. D., & Bahcall, J. N. 1987, ApJ, 317, 637
Kylafis, N. D., & Xilouris, E. M. 2005, in The Spectral Energy Distributions of Gas-Rich Galaxies: Confronting Models with Data, Heidelberg, 4−8 Oct., 2004, ed. C. C. Popescu, & R. J. Tuffs, AIP Conf. Ser., 761, 3
Lilly, S., Schade, D., Ellis, R., et al. 1998, ApJ, 500, 75
MacArthur, L. A., Courteau, S., & Holtzman, J. A. 2003, ApJ, 582, 689
Marleau, F. R., & Simard, L. 1998, ApJ, 507, 585
Meijerink, R., Tilanus, R. P. J., Dullemond, C. P., Israel, F. P., & van der Werf, P. P. 2005, A&A, 430, 427
Misiriotis, A., & Bianchi, S. 2002, A&A, 384, 866
Misiriotis, A., Popescu, C. C., Tuffs, R. J., & Kylafis, N. D. 2001, A&A, 372, 775
Misiriotis, A., Papadakis, I. E., Kylafis, N. D., & Papamastorakis, J. 2004, A&A, 417, 39

Mo, H. J., Mao, S., & White, S. D. M. 1998, MNRAS, 295, 319

Möllenhoff, C. 2004, A&A, 415, 63

Möllenhoff, C., & Heidt, J. 2001, A&A, 368, 16

Pei, Y., Fall, S. M., & Hauser, M. G. 1999, ApJ, 522, 604

Peletier, R. F., Valentijn, E. A., Moorwood, A. F. M., & Freudling, W. 1994, A&AS, 108, 621

Peng, C. Y., Ho, L. C., Impey, C. D., & Rix, H.-W. 2002, AJ, 124, 266

Pierini, D., & Tuffs, R. J. 1999, A&A, 343, 751

Pierini, D., Gordon, K. D., Witt, A. N., & Madsen, G. J. 2004, ApJ, 617, 1022

Pierini, D., Maraston, C., Gordon, K. D., & Witt, A. N. 2005, MNRAS, 363, 131

Pompei, E., & Natali, G. 1997, A&AS, 124, 129

Popescu, C. C., & Tuffs, R. J. 2005, in The Spectral Energy Distribution of Gas-Rich Galaxies: Confronting Models with Data, Heidelberg, 4−8 Oct. 2004, ed. C. C. Popescu, & R. J. Tuffs, AIP Conf. Ser., 761, 155

Popescu, C. C., Misiriotis A., Kylafis, N. D., Tuffs, R. J., & Fischera, J. 2000, A&A, 362, 138

Popescu, C. C., Tuffs, R. J., Völk, H. J., Pierini, D., & Madore, B. F. 2002, ApJ, 567, 221

Popescu, C. C., Tuffs, R. J., Kylafis, N. D., & Madore, B. F. 2004, A&A, 414, 45

Prieto, M., Aguerri, J. A. L., Varela, A. M., & Muñoz-Tuñón, C. 2001, A&A, 367, 405

Ravindranath, S., Ferguson, H. C., Conselice, C., et al. 2004, ApJ, 604, L9

Simard, L. 1998, ASPC, 145, 108

Simard, L., Koo, D. C., Faber, S. M., et al. 1999, ApJ, 519, 563

Trujillo, I., & Aguerri, J. A. L. 2004, MNRAS, 355, 82

Trujillo, I., Förster Schreiber, N. M., Rudnick, G., et al. 2005, ApJ, submitted

Tuffs, R. J., Popescu, C. C., Pierini, D., et al. 2002a, ApJS, 139, 37

Tuffs, R. J., Popescu, C. C., Pierini, D., et al. 2002b, ApJS, 140, 609

Tuffs, R. J., Popescu, C. C., Völk, H. J., Kylafis, N. D., & Dopita, M. A. 2004, A&A, 419, 835

Xilouris, E. M., Byun, Y. I., Kylafis, N. D., Paleologou, E. V., & Papamastorakis, J. 1999, A&A, 344, 868

Online Material

Table 1. Structural parameters of the disks in *B*.

i	τ_B^f	Q_{app}	$\frac{R_{app}}{R_0}$	$\frac{I_{app}^c}{I_0^c}$	ΔSB
0	0.1	1.000	0.995	1.005	−0.001
0	0.3	1.000	1.002	0.997	0.020
0	0.5	1.000	1.013	0.977	0.056
0	1.0	1.000	1.048	0.907	0.171
0	2.0	1.000	1.129	0.765	0.428
0	4.0	1.000	1.276	0.559	0.815
0	8.0	1.000	1.438	0.378	1.161
26	0.1	0.899	0.996	1.125	−0.110
26	0.3	0.899	1.004	1.109	−0.081
26	0.5	0.898	1.016	1.082	−0.039
26	1.0	0.897	1.055	0.997	0.093
26	2.0	0.895	1.147	0.820	0.380
26	4.0	0.890	1.306	0.585	0.776
26	8.0	0.882	1.456	0.397	1.103
37	0.1	0.799	0.997	1.247	−0.210
37	0.3	0.799	1.008	1.220	−0.172
37	0.5	0.799	1.024	1.181	−0.120
37	1.0	0.798	1.070	1.068	0.031
37	2.0	0.795	1.166	0.866	0.321
37	4.0	0.788	1.316	0.621	0.696
37	8.0	0.778	1.448	0.428	1.012
46	0.1	0.701	0.999	1.426	−0.343
46	0.3	0.701	1.014	1.386	−0.294
46	0.5	0.700	1.034	1.331	−0.232
46	1.0	0.699	1.087	1.184	−0.060
46	2.0	0.694	1.192	0.938	0.256
46	4.0	0.685	1.345	0.662	0.626
46	8.0	0.676	1.465	0.458	0.932
53	0.1	0.604	1.002	1.644	−0.483
53	0.3	0.603	1.021	1.580	−0.420
53	0.5	0.603	1.043	1.502	−0.346
53	1.0	0.601	1.103	1.316	−0.154
53	2.0	0.596	1.216	1.022	0.171
53	4.0	0.587	1.365	0.719	0.531
53	8.0	0.578	1.477	0.499	0.841
60	0.1	0.507	1.007	1.927	−0.637
60	0.3	0.506	1.032	1.822	−0.553
60	0.5	0.506	1.060	1.708	−0.459
60	1.0	0.503	1.134	1.446	−0.231
60	2.0	0.498	1.259	1.089	0.103
60	4.0	0.490	1.403	0.760	0.441
60	8.0	0.483	1.480	0.540	0.737
66	0.1	0.410	1.017	2.366	−0.836
66	0.3	0.409	1.056	2.161	−0.706
66	0.5	0.408	1.095	1.974	−0.583
66	1.0	0.405	1.181	1.609	−0.324
66	2.0	0.400	1.309	1.183	0.002
66	4.0	0.392	1.422	0.841	0.315
66	8.0	0.388	1.475	0.606	0.626
73	0.1	0.315	1.028	2.982	−1.055
73	0.3	0.314	1.077	2.651	−0.893
73	0.5	0.312	1.124	2.369	−0.748
73	1.0	0.310	1.222	1.866	−0.469
73	2.0	0.304	1.349	1.350	−0.140
73	4.0	0.298	1.453	0.956	0.177
73	8.0	0.295	1.492	0.687	0.499

Table 2. Structural parameters of the disks in *V*.

i	τ_B^f	Q_{app}	$\frac{R_{app}}{R_0}$	$\frac{I_{app}^c}{I_0^c}$	ΔSB
0	0.1	1.000	0.996	1.004	−0.001
0	0.3	1.000	0.999	1.002	0.010
0	0.5	1.000	1.006	0.991	0.032
0	1.0	1.000	1.029	0.947	0.108
0	2.0	1.000	1.087	0.837	0.296
0	4.0	1.000	1.208	0.647	0.644
0	8.0	1.000	1.376	0.443	1.031
26	0.1	0.900	0.996	1.125	−0.112
26	0.3	0.900	1.001	1.118	−0.095
26	0.5	0.900	1.010	1.101	−0.067
26	1.0	0.899	1.037	1.041	0.024
26	2.0	0.898	1.104	0.902	0.242
26	4.0	0.894	1.235	0.678	0.612
26	8.0	0.888	1.401	0.461	0.974
37	0.1	0.800	0.998	1.248	−0.212
37	0.3	0.800	1.005	1.233	−0.189
37	0.5	0.800	1.016	1.207	−0.155
37	1.0	0.799	1.048	1.127	−0.050
37	2.0	0.797	1.118	0.964	0.174
37	4.0	0.793	1.246	0.724	0.530
37	8.0	0.785	1.395	0.499	0.883
46	0.1	0.702	1.000	1.426	−0.344
46	0.3	0.702	1.010	1.400	−0.312
46	0.5	0.702	1.023	1.362	−0.268
46	1.0	0.701	1.062	1.251	−0.143
46	2.0	0.698	1.144	1.043	0.111
46	4.0	0.692	1.282	0.765	0.474
46	8.0	0.683	1.418	0.529	0.805
53	0.1	0.604	1.002	1.644	−0.484
53	0.3	0.604	1.015	1.601	−0.441
53	0.5	0.604	1.031	1.545	−0.388
53	1.0	0.603	1.075	1.400	−0.245
53	2.0	0.600	1.164	1.143	0.028
53	4.0	0.594	1.306	0.826	0.389
53	8.0	0.586	1.434	0.572	0.715
60	0.1	0.508	1.007	1.933	−0.642
60	0.3	0.508	1.024	1.857	−0.581
60	0.5	0.507	1.046	1.770	−0.512
60	1.0	0.506	1.101	1.557	−0.336
60	2.0	0.503	1.202	1.231	−0.042
60	4.0	0.496	1.339	0.880	0.304
60	8.0	0.489	1.444	0.618	0.609
66	0.1	0.412	1.015	2.379	−0.844
66	0.3	0.411	1.044	2.224	−0.747
66	0.5	0.410	1.074	2.073	−0.651
66	1.0	0.408	1.143	1.757	−0.437
66	2.0	0.404	1.253	1.343	−0.131
66	4.0	0.398	1.378	0.958	0.193
66	8.0	0.393	1.451	0.687	0.494
73	0.1	0.316	1.025	3.006	−1.066
73	0.3	0.315	1.061	2.747	−0.943
73	0.5	0.315	1.097	2.514	−0.827
73	1.0	0.312	1.178	2.062	−0.586
73	2.0	0.308	1.295	1.536	−0.272
73	4.0	0.302	1.410	1.089	0.053
73	8.0	0.298	1.470	0.781	0.364

Table 3. Structural parameters of the disks in *I*.

i	τ_B^{f}	Q_{app}	$\frac{R_{\mathrm{app}}}{R_0}$	$\frac{I_{\mathrm{app}}^{\mathrm{c}}}{I_0^{\mathrm{c}}}$	ΔSB
0	0.1	1.000	0.996	1.007	−0.006
0	0.3	1.000	0.998	1.007	−0.001
0	0.5	1.000	1.000	1.003	0.009
0	1.0	1.000	1.011	0.982	0.046
0	2.0	1.000	1.043	0.919	0.148
0	4.0	1.000	1.117	0.780	0.379
0	8.0	1.000	1.248	0.575	0.751
26	0.1	0.900	1.003	1.116	−0.103
26	0.3	0.900	1.006	1.114	−0.095
26	0.5	0.900	1.011	1.107	−0.082
26	1.0	0.899	1.026	1.075	−0.034
26	2.0	0.899	1.065	0.989	0.089
26	4.0	0.899	1.147	0.818	0.345
26	8.0	0.897	1.282	0.590	0.717
37	0.1	0.803	0.998	1.253	−0.218
37	0.3	0.803	1.002	1.246	−0.206
37	0.5	0.803	1.008	1.233	−0.187
37	1.0	0.803	1.026	1.186	−0.128
37	2.0	0.802	1.068	1.077	0.011
37	4.0	0.801	1.156	0.878	0.286
37	8.0	0.798	1.293	0.630	0.655
46	0.1	0.705	1.003	1.419	−0.338
46	0.3	0.705	1.008	1.404	−0.319
46	0.5	0.705	1.015	1.384	−0.297
46	1.0	0.705	1.036	1.320	−0.227
46	2.0	0.704	1.086	1.179	−0.069
46	4.0	0.701	1.184	0.938	0.221
46	8.0	0.697	1.321	0.664	0.584
53	0.1	0.608	1.005	1.641	−0.478
53	0.3	0.608	1.013	1.614	−0.453
53	0.5	0.608	1.022	1.580	−0.422
53	1.0	0.607	1.049	1.485	−0.336
53	2.0	0.606	1.106	1.296	−0.155
53	4.0	0.604	1.211	1.008	0.157
53	8.0	0.599	1.344	0.709	0.513
60	0.1	0.512	1.007	1.939	−0.641
60	0.3	0.512	1.019	1.890	−0.604
60	0.5	0.512	1.032	1.834	−0.563
60	1.0	0.511	1.066	1.690	−0.453
60	2.0	0.509	1.132	1.437	−0.246
60	4.0	0.506	1.240	1.094	0.068
60	8.0	0.501	1.363	0.770	0.405
66	0.1	0.415	1.018	2.362	−0.832
66	0.3	0.415	1.034	2.268	−0.778
66	0.5	0.415	1.051	2.173	−0.722
66	1.0	0.414	1.093	1.950	−0.584
66	2.0	0.412	1.171	1.598	−0.348
66	4.0	0.408	1.284	1.179	−0.024
66	8.0	0.403	1.387	0.833	0.301
73	0.1	0.320	1.024	3.012	−1.066
73	0.3	0.320	1.048	2.831	−0.985
73	0.5	0.320	1.072	2.663	−0.905
73	1.0	0.318	1.128	2.308	−0.729
73	2.0	0.316	1.218	1.822	−0.461
73	4.0	0.312	1.329	1.326	−0.142
73	8.0	0.307	1.411	0.948	0.167

Table 4. Structural parameters of the disks in *J*.

i	τ_B^{f}	Q_{app}	$\frac{R_{\mathrm{app}}}{R_0}$	$\frac{I_{\mathrm{app}}^{\mathrm{c}}}{I_0^{\mathrm{c}}}$	ΔSB
0	0.1	1.000	1.001	1.000	0.001
0	0.3	1.000	1.003	0.999	0.005
0	0.5	1.000	1.005	0.996	0.011
0	1.0	1.000	1.012	0.985	0.030
0	2.0	1.000	1.027	0.952	0.079
0	4.0	1.000	1.061	0.877	0.193
0	8.0	1.000	1.131	0.737	0.420
26	0.1	0.902	1.002	1.119	−0.106
26	0.3	0.902	1.004	1.115	−0.099
26	0.5	0.902	1.007	1.110	−0.091
26	1.0	0.902	1.015	1.092	−0.065
26	2.0	0.901	1.033	1.047	−0.005
26	4.0	0.901	1.075	0.947	0.132
26	8.0	0.900	1.158	0.772	0.392
37	0.1	0.804	1.003	1.239	−0.202
37	0.3	0.804	1.006	1.233	−0.194
37	0.5	0.804	1.009	1.226	−0.185
37	1.0	0.804	1.018	1.203	−0.157
37	2.0	0.804	1.038	1.147	−0.091
37	4.0	0.803	1.081	1.030	0.050
37	8.0	0.803	1.161	0.837	0.308
46	0.1	0.707	1.005	1.415	−0.330
46	0.3	0.707	1.009	1.403	−0.319
46	0.5	0.708	1.013	1.391	−0.306
46	1.0	0.707	1.024	1.354	−0.268
46	2.0	0.707	1.049	1.274	−0.186
46	4.0	0.706	1.099	1.121	−0.021
46	8.0	0.704	1.189	0.886	0.261
53	0.1	0.610	1.007	1.633	−0.470
53	0.3	0.610	1.012	1.613	−0.453
53	0.5	0.610	1.017	1.593	−0.436
53	1.0	0.610	1.030	1.540	−0.390
53	2.0	0.610	1.058	1.432	−0.294
53	4.0	0.609	1.115	1.237	−0.109
53	8.0	0.607	1.211	0.957	0.188
60	0.1	0.515	1.011	1.920	−0.627
60	0.3	0.514	1.017	1.891	−0.606
60	0.5	0.514	1.024	1.861	−0.585
60	1.0	0.514	1.040	1.782	−0.528
60	2.0	0.514	1.074	1.630	−0.414
60	4.0	0.512	1.137	1.376	−0.208
60	8.0	0.510	1.237	1.044	0.097
66	0.1	0.419	1.017	2.365	−0.832
66	0.3	0.419	1.026	2.305	−0.797
66	0.5	0.419	1.036	2.245	−0.762
66	1.0	0.418	1.060	2.103	−0.677
66	2.0	0.418	1.107	1.855	−0.522
66	4.0	0.415	1.185	1.495	−0.277
66	8.0	0.412	1.286	1.102	0.031
73	0.1	0.325	1.025	2.992	−1.056
73	0.3	0.325	1.037	2.894	−1.013
73	0.5	0.325	1.048	2.800	−0.970
73	1.0	0.324	1.077	2.584	−0.870
73	2.0	0.323	1.130	2.230	−0.694
73	4.0	0.321	1.215	1.752	−0.433
73	8.0	0.316	1.315	1.270	−0.116

Table 5. Structural parameters of the disks in K.

i	τ_B^f	Q_{app}	$\frac{R_{app}}{R_0}$	$\frac{I_{app}^c}{I_0^c}$	ΔSB
0	0.1	1.000	1.002	0.998	0.002
0	0.3	1.000	1.003	0.995	0.006
0	0.5	1.000	1.005	0.992	0.011
0	1.0	1.000	1.008	0.984	0.022
0	2.0	1.000	1.014	0.967	0.045
0	4.0	1.000	1.027	0.933	0.091
0	8.0	1.000	1.054	0.865	0.188
26	0.1	0.903	1.003	1.117	−0.101
26	0.3	0.903	1.005	1.112	−0.096
26	0.5	0.903	1.006	1.108	−0.090
26	1.0	0.903	1.010	1.096	−0.076
26	2.0	0.903	1.018	1.072	−0.047
26	4.0	0.902	1.035	1.024	0.012
26	8.0	0.902	1.067	0.933	0.127
37	0.1	0.806	1.004	1.236	−0.195
37	0.3	0.806	1.006	1.231	−0.189
37	0.5	0.806	1.007	1.225	−0.184
37	1.0	0.806	1.011	1.212	−0.170
37	2.0	0.806	1.019	1.186	−0.142
37	4.0	0.806	1.034	1.134	−0.085
37	8.0	0.806	1.066	1.036	0.028
46	0.1	0.710	1.006	1.410	−0.321
46	0.3	0.710	1.008	1.402	−0.314
46	0.5	0.710	1.010	1.395	−0.307
46	1.0	0.709	1.015	1.375	−0.289
46	2.0	0.709	1.025	1.337	−0.253
46	4.0	0.709	1.045	1.263	−0.182
46	8.0	0.709	1.083	1.129	−0.045
53	0.1	0.613	1.008	1.627	−0.459
53	0.3	0.613	1.010	1.617	−0.450
53	0.5	0.613	1.013	1.606	−0.442
53	1.0	0.613	1.019	1.580	−0.421
53	2.0	0.613	1.030	1.528	−0.379
53	4.0	0.613	1.053	1.430	−0.297
53	8.0	0.613	1.096	1.260	−0.144
60	0.1	0.519	1.012	1.910	−0.612
60	0.3	0.518	1.014	1.895	−0.602
60	0.5	0.518	1.017	1.881	−0.593
60	1.0	0.518	1.023	1.845	−0.569
60	2.0	0.518	1.036	1.776	−0.521
60	4.0	0.518	1.061	1.647	−0.429
60	8.0	0.517	1.109	1.431	−0.261
66	0.1	0.424	1.017	2.350	−0.817
66	0.3	0.424	1.021	2.323	−0.802
66	0.5	0.424	1.025	2.296	−0.787
66	1.0	0.424	1.035	2.231	−0.750
66	2.0	0.424	1.053	2.110	−0.679
66	4.0	0.423	1.089	1.898	−0.549
66	8.0	0.422	1.150	1.578	−0.337
73	0.1	0.331	1.026	2.960	−1.036
73	0.3	0.331	1.031	2.919	−1.019
73	0.5	0.331	1.035	2.881	−1.002
73	1.0	0.331	1.046	2.787	−0.961
73	2.0	0.330	1.067	2.614	−0.882
73	4.0	0.330	1.106	2.320	−0.739
73	8.0	0.328	1.173	1.892	−0.512